# Steady-state plasma model of an iodine-fueled Hall thruster

Pascal Chabert, Anne Bourdon, Benjamin Esteves, Trevor Lafleur

Journal of Applied Physics



AIP Publishing

# Steady-State Plasma Model of an Iodine-Fueled Hall Thruster

Pascal Chabert* and Anne Bourdon

*LPP, CNRS, Ecole Polytechnique,*

*Sorbonne Université,* 91128 *Palaiseau, France*

Benjamin Esteves

*Safran Spacecraft Propulsion, Vernon, Normandie, 27200, France*

T. Lafleur

*School of Engineering and Technology,*

*University of New South Wales Canberra, Canberra,*

*2600, Australian Capital Territory, Australia*

## Abstract

A time-independent one-dimensional plasma model is proposed and used to investigate the characteristics and performance of iodine-fueled Hall thrusters. The model accounts for radial plasma-wall losses and includes major iodine collisional reaction processes such as molecular dissociation. Thruster performance is found to be comparable to that obtained with xenon, although iodine allows extension of the operating range to lower mass flow rates and discharge voltages. The model predicts an appreciable fraction of molecular ions ($I_2^+$) within the thruster plume that depends on the discharge voltage and propellant mass flow rate, and which contributes significantly to the thrust. In contrast to xenon, electron impact dissociation of iodine leads to the unique formation of two distinct ionization zones within the thruster: a region closer to the anode associated with the ionization of molecular iodine and a downstream region associated with the ionization of atomic iodine.

* pascal.chabert@lpp.polytechnique.fr

## I. INTRODUCTION

The space industry has experienced rapid growth over the last ten years that is set to continue into the foreseeable future [1]. Important drivers of this growth include reduced launch costs [2], the trend towards smaller satellites [3], and the rise of satellite constellations [4] in low-Earth orbit providing services such as low-latency communication [5] and Earth observation [3]. To enable in-space mobility, many satellites require an onboard propulsion system, with plasma-based electric thrusters being particularly attractive because of their high performance [6, 7]. Hall thrusters are currently the most prevalent electric propulsion technology and have been developed for more than 50 years [6–8]. However, despite their high level of maturity, Hall thrusters remain an important research topic because of continually emerging commercial and space mission needs. For example, there is growing interest in extending thruster operation to both lower and higher power levels, and in the use of alternative propellants [9–11]. Because of the complex underlying physics though, Hall thruster design is still largely empirical [12, 13], and development of new thrusters is a long and costly process.

As with other complex engineering devices, Hall thruster design and optimization benefits from numerical simulations. Because of the specific geometry of Hall thrusters, and their unique $\mathbf{E} \times \mathbf{B}$ configuration [14], high-fidelity simulation models in principle need to be three-dimensional. Firstly, it is important to model the thrust direction (which is parallel to the cylindrical axis of the thruster channel) to determine thruster performance and account for the strong axial gradients that are present in almost all plasma properties. Secondly, plasma losses to the radial channel walls affect both the ionization and power balance of the system, and lead to secondary electron emission [7, 15]. Finally, the applied electric and magnetic fields result in an electron drift in the azimuthal direction that can drive large-amplitude kinetic instabilities, such as the Electron Cyclotron Drift Instability (ECDI), which have been implicated in anomalous cross-field electron transport [14, 16–19]. Because of the kinetic nature of such instabilities, modeling of Hall thrusters with a fluid formalism fails to predict anomalous transport. While some simplified phenomenological transport models have been proposed [20–24], they require experimentally-derived coefficients. Several attempts to obtain reliable first principles transport models have been made [19, 25], but they are challenging to self-consistently incorporate into fluid simulations. This would suggest

that three-dimensional kinetic simulations, such as Particle-In-Cell (PIC) simulations, are ultimately necessary, but such simulations are computationally intensive and are not yet feasible for practical thruster design. Consequently, simplified models and compromises are necessary.

Several fluid or hybrid models have been developed within the community and which include time-varying one-dimensional models that reproduce the low-frequency breathing mode oscillations [20, 22, 26], time-independent models focused on steady-state operation and thruster performance [27–29], and higher fidelity two-dimensional models providing a more accurate and complete description of Hall thrusters [21, 23, 24]. A number of simplified models have also been developed to better understand thruster scaling and similarity laws [12, 13, 30]. This includes the analytical model in Ref. [31], and the more recent numerical model in Ref. [32] that directly identified the main similarity parameters governing Hall thruster operation. This latter model was shown to be in good agreement with experiment measurements and was able to predict several existing scaling laws and thruster designs at low ($\sim$ 100 W), medium ($\sim$ 1 kW), and high power ($\sim$ 20 kW).

Most previously developed models have been derived for noble gas propellants, such as xenon, and only included single neutral (i.e. gas atoms) and singly-charged atomic ion species. Although xenon has historically been the propellant of choice for Hall thrusters due to its relatively low ionization threshold energy, high atomic mass, and reasonably high storage density, xenon is expensive and the commercial market is subject to strong fluctuations [33, 34]. Indeed, estimates suggest that space industry demand alone may outpace supply in the near future [35]. Consequently, the space industry has been investigating alternative propellants including other noble gases such as krypton and argon [36], as well as condensable propellants like iodine [9, 11, 37–39] or metals [9, 40]. Iodine in particular has been seriously studied in recent years, and in addition to being cheaper with a higher global production output [41], can be stored unpressurized as a solid. The first iodine-fueled Hall thruster was developed at least as early as 2011 [42], and ground tests demonstrated performance comparable to xenon. While an iodine Hall thruster was scheduled to be demonstrated in space as part of the iSat mission [43, 44], this was canceled partly due to concerns with the compatibility of iodine with existing hollow cathode neutralizers. Iodine gridded ion thrusters have however been demonstrated in space since 2020 [35]. Both ground and space testing has also validated existing iodine plasma models for gridded ion thrusters, and shown that

existing iodine plasma chemistry sets and collision cross-section data appear reasonable [45]. However, there has been very little modeling of iodine Hall thrusters performed, and given the unique plasma chemistry of iodine [46, 47], and the strong axial gradients that exist in Hall thrusters [7, 48], significant changes to the resulting plasma structure and behavior are expected compared with both noble gas propellants and gridded ion thrusters. Bianchi et al. [49] proposed a zero-dimensional global model (somewhat similar to those developed for iodine gridded ion thrusters [47, 50–53]), but this model did not account for axial gradients. It did however highlight the likely importance of iodine dissociation and the formation of an appreciable fraction of molecular ions.

The present paper aims to extend the previous work in Ref. [32] to iodine propellant. Because of the differences between iodine and xenon plasma chemistry, important changes to the discharge structure and composition emerge as both molecular and atomic neutral and positive ion species can be generated. The paper is organized as follows. The mathematical model and proposed iodine plasma chemistry set is described in Sec. II, while results are presented in Sec. III. A discussion of the model and several conclusions are then given in Sec. IV.

## II. MODEL DESCRIPTION

We consider a steady-state, one-dimensional, fluid model of a Hall thruster along the axial (thrust) direction. Plasma interactions with the radial channel walls (including ion/neutral recombination and secondary electron emission) are however accounted for using spatially-dependent loss/generation rates.

### A. Reaction set and model equations

Although many iodine collisional reaction processes are possible (see for example Refs. [47, 53]), here we use the simplified reaction set listed in Table I and only consider four heavy species: $I_2$, I, $I_2^+$, and $I^+$. Similar to our previous work [31], the near anode region is not explicitly modeled and so there is no positive ion backflow to the anode. Consequently, the axial electric field is always positive and any negative ions ($I^-$) formed in the near-anode region are prevented from traveling downstream. Therefore, negative ions are not explicitly

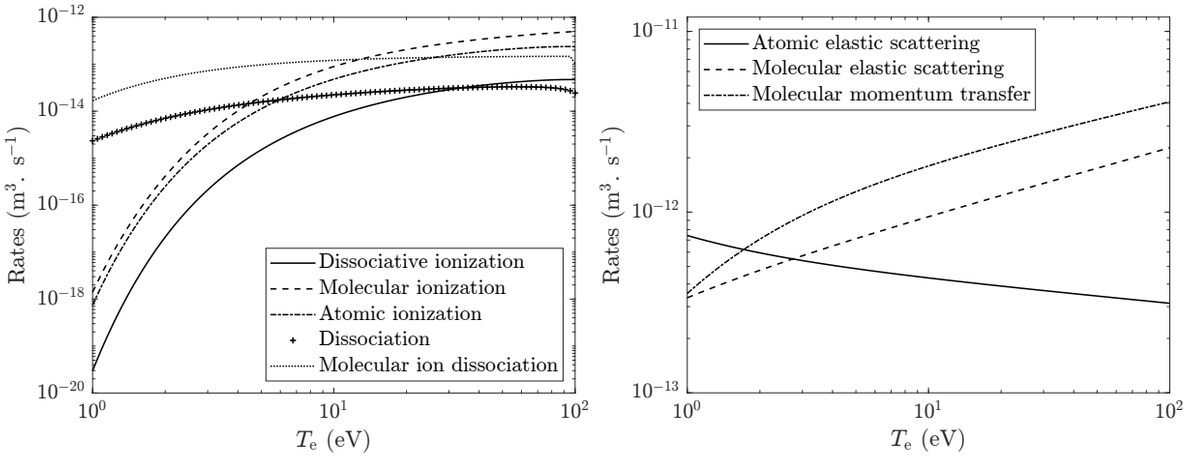


FIG. 1. Rate coefficients as a function of electron temperature for inelastic (left) and elastic (right) processes.

treated in the model, nor any dissociative attachment or detachment reaction processes [47, 53]. We also do not consider doubly-charged atomic iodine ions ($I^{2+}$), although we note that while the fraction of such ions is negligible in gridded ion thrusters [53], they could play a more important role in Hall thrusters because of the higher electron temperature. Figure 1 shows the rate coefficients used in the model as a function of electron temperature (assuming a Maxwellian distribution), and which are determined with cross-section data from Refs. [46, 47]. As momentum transfer cross-sections are unavailable for atomic iodine, we use the elastic scattering cross-sections instead [46].

TABLE I. Simplified reaction set used in the model.

| Reaction | Process | Rate | Threshold (eV) | Ref. |
|---|---|---|---|---|
| $I_2 + e^- \longrightarrow I_2 + e^-$ | Momentum transfer | $K_{m,I_2}$ | - | [46] |
| $I_2 + e^- \longrightarrow I_2^+ + 2e^-$ | Ionization | $K_{iz,I_2}$ | 9.31 | [46] |
| $I_2 + e^- \longrightarrow I^+ + I + 2e^-$ | Dissociative ionization | $K_{diss.iz,I_2}$ | 11.94 | [46] |
| $I_2 + e^- \longrightarrow 2I + e^-$ | Dissociation | $K_{diss,I_2}$ | 1.542 | [47] |
| $I + e^- \longrightarrow I^+ + 2e^-$ | Ionization | $K_{iz,I}$ | 10.45 | [46] |
| $I + e^- \longrightarrow I + e^-$ | Elastic scattering | $K_{el,I}$ | - | [46] |
| $I_2^+ + e^- \longrightarrow I^+ + I + e^-$ | Molecular ion dissociation | $K_{diss,I_2^+}$ | 2.18 | [47] |

The continuity equations for each species in the model are given by

$$\frac{\mathrm{d}}{\mathrm{d}x}\left(n_{\mathrm{I}_2}v_{\mathrm{I}_2}\right) = -n_{\mathrm{e}}n_{\mathrm{I}_2}\left(K_{\mathrm{iz,I}_2}+K_{\mathrm{diss.iz,I}_2}+K_{\mathrm{diss,I}_2}\right) + \frac{1}{4}n_{\mathrm{I}}\sqrt{\frac{8}{\pi}}v_{\mathrm{I}}\left(\frac{2\gamma}{2-\gamma}\right)\left(\frac{1}{\Delta R}\right)+\frac{2h_R n_{\mathrm{I}_2^+}u_{\mathrm{B,I}_2^+}}{\Delta R}, \quad (1)$$

$$\frac{\mathrm{d}}{\mathrm{d}x}\left(n_{\mathrm{I}}v_{\mathrm{I}}\right) = n_{\mathrm{e}}n_{\mathrm{I}_2}\left(K_{\mathrm{diss.iz,I}_2}+2K_{\mathrm{diss,I}_2}\right)-n_{\mathrm{e}}n_{\mathrm{I}}K_{\mathrm{iz,I}}+n_{\mathrm{e}}n_{\mathrm{I}_2^+}K_{\mathrm{diss,I}_2^+} - \frac{1}{4}n_{\mathrm{I}}\sqrt{\frac{8}{\pi}}v_{\mathrm{I}}\left(\frac{2\gamma}{2-\gamma}\right)\left(\frac{2}{\Delta R}\right)+\frac{2h_R n_{\mathrm{I}^+}u_{\mathrm{B,I}^+}}{\Delta R}, \quad (2)$$

$$\frac{\mathrm{d}}{\mathrm{d}x}\left(n_{\mathrm{I}_2^+}v_{\mathrm{I}_2^+}\right) = n_{\mathrm{e}}n_{\mathrm{I}_2}K_{\mathrm{iz,I}_2}-n_{\mathrm{e}}n_{\mathrm{I}_2^+}K_{\mathrm{diss,I}_2^+}-\frac{2h_R n_{\mathrm{I}_2^+}u_{\mathrm{B,I}_2^+}}{\Delta R}, \quad (3)$$

$$\frac{\mathrm{d}}{\mathrm{d}x}\left(n_{\mathrm{I}^+}v_{\mathrm{I}^+}\right) = n_{\mathrm{e}}n_{\mathrm{I}}K_{\mathrm{iz,I}}+n_{\mathrm{e}}n_{\mathrm{I}_2}K_{\mathrm{diss.iz,I}_2}+n_{\mathrm{e}}n_{\mathrm{I}_2^+}K_{\mathrm{diss,I}_2^+}-\frac{2h_R n_{\mathrm{I}^+}u_{\mathrm{B,I}^+}}{\Delta R}, \quad (4)$$

$$\frac{\mathrm{d}}{\mathrm{d}x}\left(n_{\mathrm{e}}v_{\mathrm{e},x}\right) = n_{\mathrm{e}}n_{\mathrm{I}_2}\left(K_{\mathrm{iz,I}_2}+K_{\mathrm{diss.iz,I}_2}\right)+n_{\mathrm{e}}n_{\mathrm{I}}K_{\mathrm{iz,I}}-\frac{2h_R}{\Delta R}\left(n_{\mathrm{I}^+}u_{\mathrm{B,I}^+}+n_{\mathrm{I}_2^+}u_{\mathrm{B,I}_2^+}\right), \quad (5)$$

where $n_{\mathrm{I}_2}$ and $n_{\mathrm{I}}$ are the molecular and atomic neutral densities, $n_{\mathrm{I}_2^+}$ and $n_{\mathrm{I}^+}$ are the corresponding molecular and atomic ion densities, and $n_{\mathrm{e}}$ is the electron density. The plasma is assumed to be quasi-neutral such that $n_{\mathrm{e}} = n_{\mathrm{I}_2^+}+n_{\mathrm{I}^+}$. The axial electron fluid velocity, $v_{\mathrm{e},x}$, and ion fluid velocities, $v_{\mathrm{I}_2^+}$ and $v_{\mathrm{I}^+}$, are all functions of $x$, while the neutral fluid velocities are assumed constant and equal to their corresponding thermal velocities defined as

$$v_{\mathrm{I}_2} = \sqrt{\frac{k_{\mathrm{B}}T_{\mathrm{g}}}{2M}}, \quad (6)$$

$$v_{\mathrm{I}} = \sqrt{\frac{k_{\mathrm{B}}T_{\mathrm{g}}}{M}}, \quad (7)$$

where $M = 126.9$ u is the atomic mass of iodine in unified atomic mass units, $k_{\mathrm{B}}$ is Boltzmann's constant, and $T_{\mathrm{g}} = 700$ K (representative of measured channel wall temperatures in Ref. [54]) is a constant gas temperature assumed equal for both molecules and atoms. The continuity equations include radial ion and electron loss terms in which $h_R$ is the so-called radial edge-to-center density ratio [55] and $\Delta R = R_{\mathrm{out}} - R_{\mathrm{in}}$ is the channel width with $R_{\mathrm{in}}$ and $R_{\mathrm{out}}$ the inner and outer channel radii respectively. In the low pressure limit, $h_R \approx 0.4$ for a cylindrical geometry [55], although as discussed in Ref. [32], a slightly better fit with xenon and krypton experimental data is obtained with $h_R = 0.3$ because of model assumptions (such as neglect of ion focusing due to the two-dimensional magnetic field topography). The formation of ion streaming instabilities in the radial presheath is ignored [56, 57] such

that atomic and molecular ions each enter the sheath with their individual Bohm velocities given by

$$u_{\mathrm{B,I_2^+}} = \sqrt{\frac{k_\mathrm{B}T_\mathrm{e}}{2M}}, \tag{8}$$

$$u_{\mathrm{B,I^+}} = \sqrt{\frac{k_\mathrm{B}T_\mathrm{e}}{M}}. \tag{9}$$

with $T_\mathrm{e}$ the electron temperature. Finally, iodine atoms recombine at the radial channel walls (with a recombination probability $\gamma$) to form iodine molecules. The net (radial) iodine atomic flux is

$$\Gamma_\mathrm{net,I} = \frac{1}{4}n_\mathrm{I}\overline{v}_\mathrm{I}\left(\frac{2\gamma}{2-\gamma}\right), \tag{10}$$

$$= \frac{1}{4}n_\mathrm{I}\sqrt{\frac{8}{\pi}}v_\mathrm{I}\left(\frac{2\gamma}{2-\gamma}\right), \tag{11}$$

where $\bar{v}_\mathrm{I} = \sqrt{8k_\mathrm{B}T_\mathrm{g}/\pi M} = v_\mathrm{I}\sqrt{8/\pi}$. As discussed in Refs. [47, 53], the surface recombination probability depends sensitively on the wall material and surface state, with measured values between 0.001-0.2. We therefore use a representative value of $\gamma = 0.1$.

The system of five differential equations above can be reduced thanks to overall mass conservation in the thruster. By multiplying Eqs. (46) and (47) by two (since the mass of molecular iodine is twice that of atomic iodine) and adding the result to the sum of Eqs. (2) and (48), we obtain

$$2\Gamma_{\mathrm{I}_2} + \Gamma_\mathrm{I} + 2\Gamma_{\mathrm{I}_2^+} + \Gamma_{\mathrm{I}^+} = 2\Gamma_{\mathrm{I}_2,\mathrm{inj}}, \tag{12}$$

where the flux of a given species $i$ is $\Gamma_i = n_i v_i$, and $\Gamma_{\mathrm{I}_2,\mathrm{inj}} = Q_\mathrm{m}/(2MA_\mathrm{ch})$ is a constant with $Q_\mathrm{m}$ the initial molecular iodine mass flow rate injected at the anode, and $A_\mathrm{ch} = \pi\left(R_\mathrm{out}^2 - R_\mathrm{in}^2\right)$ the channel cross-sectional area. The discharge current, $I_\mathrm{d}$, must also be conserved and so by adding Eqs. (47) and (48), and subtracting Eq. (5), we obtain

$$\frac{I_\mathrm{d}}{eA_\mathrm{ch}} = \Gamma_{\mathrm{I}_2^+} + \Gamma_{\mathrm{I}^+} - \Gamma_\mathrm{e}$$

$$= \Gamma_{\mathrm{I}_2^+} + \Gamma_{\mathrm{I}^+} + n_\mathrm{e}\mu E, \tag{13}$$

In Eq. 13, the electron flux has been expressed as a function of the axial electric field, $E$, and the electron mobility, $\mu$, which is determined from simplified electron momentum conservation equations in the axial, $x$, and azimuthal, $y$, directions:

$$en_{\mathrm{e}}v_{\mathrm{e},x}B = n_{\mathrm{e}}v_{\mathrm{e},y}m_{\mathrm{e}}\nu_{\mathrm{eff}}, \tag{14}$$

$$0 = -en_{\mathrm{e}}E - en_{\mathrm{e}}v_{\mathrm{e},y}B - n_{\mathrm{e}}v_{\mathrm{e},x}m_{\mathrm{e}}\nu_{\mathrm{eff}}. \tag{15}$$

with $e$ the elementary charge, $m_{\mathrm{e}}$ the electron mass, $B$ the radial magnetic field strength, and $v_{\mathrm{e},y}$ the azimuthal electron fluid velocity. As in several previous works [20–22], we use an effective collision frequency that phenomenologically accounts for anomalous electron transport

$$\nu_{\mathrm{eff}} = \nu_{\mathrm{m}} + \delta_{\mathrm{an}}\omega_{\mathrm{ce}} \tag{16}$$

$$= n_{\mathrm{I}_2}K_{\mathrm{m,I}_2} + n_{\mathrm{I}}K_{\mathrm{el,I}} + \delta_{\mathrm{an}}\omega_{\mathrm{ce}}, \tag{17}$$

where $\delta_{\mathrm{an}} \approx 0.0035$ is a constant [32], $\omega_{\mathrm{ce}} = eB/m_{\mathrm{e}}$ is the (spatially-varying) electron cyclotron frequency, and $K_{\mathrm{m,I}_2}$ and $K_{\mathrm{el,I}}$ are functions of $T_{\mathrm{e}}$ as shown in Figure 1. The electron mobility is found by combining Eqs. (14) and (15), which gives

$$\mu = \frac{e}{m_{\mathrm{e}}\nu_{\mathrm{eff}}}\left(1 + \frac{\omega_{\mathrm{ce}}^2}{\nu_{\mathrm{eff}}^2}\right)^{-1} \tag{18}$$

$$\approx \frac{e\nu_{\mathrm{eff}}}{m_{\mathrm{e}}\omega_{\mathrm{ce}}^2}. \tag{19}$$

An explicit expression for the electric field is easily obtained by rearranging Eq. (13) to get

$$E = \frac{\Gamma_{\mathrm{d}} - \Gamma_{\mathrm{I}_2^+} - \Gamma_{\mathrm{I}^+}}{n_{\mathrm{e}}\mu}, \tag{20}$$

where $\Gamma_{\mathrm{d}} = I_{\mathrm{d}}/(eA_{\mathrm{ch}})$. The ion momentum conservation equations are

$$\frac{\mathrm{d}}{\mathrm{d}x}\left(2Mn_{\mathrm{I}_2^+}v_{\mathrm{I}_2^+}^2\right) = en_{\mathrm{I}_2^+}E - \frac{2h_R n_{\mathrm{I}_2^+}u_{\mathrm{B,I}_2^+}2Mv_{\mathrm{I}_2^+}}{\Delta R}, \tag{21}$$

$$\frac{\mathrm{d}}{\mathrm{d}x}\left(Mn_{\mathrm{I}^+}v_{\mathrm{I}^+}^2\right) = en_{\mathrm{I}^+}E - \frac{2h_R n_{\mathrm{I}^+}u_{\mathrm{B,I}^+}Mv_{\mathrm{I}^+}}{\Delta R}, \tag{22}$$

where the last term in both equations accounts for momentum loss at the radial channel walls. Finally, the last model equation represents electron power conservation, which we approximate as

$$\mu E^2 \;=\; \nu_{\rm wall}\varepsilon_{\rm wall} + n_{\rm I}K_{\rm iz,I}\varepsilon_{\rm c,I} + n_{\rm I_2}\left(K_{\rm iz,I_2} + K_{\rm diss.iz,I_2}\right)\varepsilon_{\rm c,I_2}, \tag{23}$$

Here we ignore axial energy transport such that power balance is local [31, 32], which is a reasonable approximation [29]. In Eq. 51, $\varepsilon_{\rm c,I}$ and $\varepsilon_{\rm c,I_2}$ are effective atomic and molecular energy loss values per electron-ion pair produced by ionization, and which account for all collisional energy losses (including electronic excitation). For convenience, these energy loss factors are determined through a best-fit of the direct calculations provided in Ref. [53] using the following expression

$$\varepsilon_{\rm c} \;=\; \left(\mathcal{A}T_{\rm e}^{-3} + \mathcal{B}T_{\rm e}^{-2} + \mathcal{C}T_{\rm e}^{-1} + \mathcal{D}\right)\exp\left(\frac{\mathcal{E}}{T_{\rm e}}\right) + \mathcal{F}, \tag{24}$$

with $T_{\rm e}$ in units of eV. Different fitting parameters are given in Table II for both $\varepsilon_{\rm c,I}$ and $\varepsilon_{\rm c,I_2}$.

TABLE II. Parameters to compute the collisional energy loss for atoms, $\varepsilon_{\rm c,I}$, and molecules, $\varepsilon_{\rm c,I_2}$, obtained through a best-fit of the calculations in Ref. [53] with Eq. 24.

| Parameter (unit) | I | $I_2$ |
|---|---|---|
| $\mathcal{A}$ (eV$^4$) | 0.0015 | 4.1118 |
| $\mathcal{B}$ (eV$^3$) | 10.1015 | -1.4700 |
| $\mathcal{C}$ (eV$^2$) | -10.6624 | 4.8800 |
| $\mathcal{D}$ (eV) | 4.6570 | -0.3841 |
| $\mathcal{E}$ (eV) | 8.0708 | 6.3447 |
| $\mathcal{F}$ (eV) | 7.8417 | 10.0124 |

The first term on the right-hand side of Eq. 51 represents electron-wall losses with $\nu_{\rm wall}$ the wall loss collision frequency, and $\varepsilon_{\rm wall}$ the average energy per electron lost at the walls given by

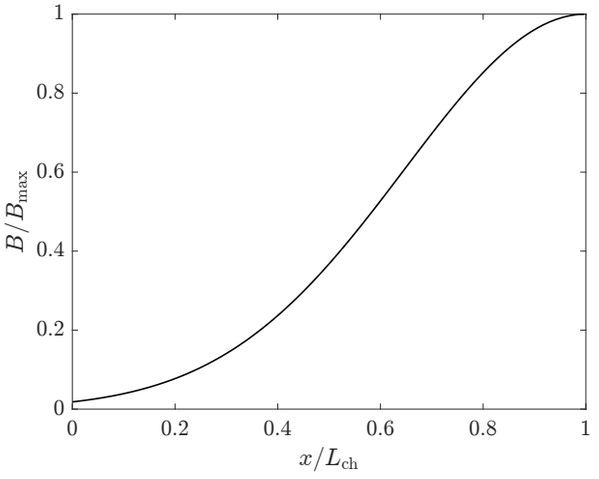


FIG. 2. Radial magnetic field profile along the thruster channel.

$$\nu_{\mathrm{wall}} = \frac{2h_R u_{\mathrm{B,I^+}}}{\beta\,(1-\sigma)\,\Delta R}, \tag{25}$$

$$\varepsilon_{\mathrm{wall}} = 2T_{\mathrm{e}} + T_{\mathrm{e}}\,(1-\sigma)\ln\left[\beta\,(1-\sigma)\sqrt{\frac{M}{2\pi m_{\mathrm{e}}}}\right], \tag{26}$$

$$\beta = \left(1+\frac{n_{\mathrm{I^+}}}{n_{\mathrm{I_2^+}}}\right)\left(\frac{1}{\sqrt{2}}+\frac{n_{\mathrm{I^+}}}{n_{\mathrm{I_2^+}}}\right)^{-1}, \tag{27}$$

$$\sigma = \min\left(\sigma_{\mathrm{cr}}, aT_{\mathrm{e}}^{b}\right), \tag{28}$$

where $\sigma$ is the electron-induced Secondary Electron Emission (SEE) yield with $\sigma_{\mathrm{cr}} \approx 0.983$ the critical yield for space-charge limited emission [7, 58], and $a = 0.207$ eV$^{-0.549}$ and $b = 0.549$ are best-fit parameters for SEE from boron nitride [7] (a typical Hall thruster channel material). The factor $\beta$ arises because the wall floating potential condition is obtained by setting the net electron flux (which includes SEE) equal to the sum of atomic and molecular ion fluxes at the radial walls. In the equations for $\varepsilon_{\mathrm{wall}}$ and $\sigma$ above, the electron temperature is again in units of eV.

### B. Numerical integration and model inputs

With the base equations and simplifications introduced in Sec. II A, the model is reduced to five ordinary differential equations and three algebraic equations that are then numerically

solved. The details of the model solving procedure are given in the appendix. The model inputs are the channel dimensions, the iodine mass flow rate at the anode, the discharge current, and the radial magnetic field profile approximated as

$$B(x) \;=\; B_{\max} \exp\left[-\frac{4\left(x - L_{\rm ch}\right)^2}{L_{\rm ch}^2}\right], \tag{29}$$

where $B_{\max}$ is the maximum magnetic field strength (and which is located at the thruster exit), and $L_{\rm ch}$ is the channel length. Figure 2 shows the axial variation of the magnetic field profile along the channel. Because of the form of the model equations, the discharge current is the more natural electrical control parameter, while the discharge voltage is essentially a model result determined by integration of the electric field,

$$V_{\rm d} \;=\; \int_0^{L_{\rm ch}} E \, {\rm d}x. \tag{30}$$

Similar to our previous work [31, 32], integration of all differential equations stops at the thruster exit and the plume region is not modeled.

### C. Outputs and performance metrics

The model provides axial profiles of all relevant discharge properties (i.e. densities, velocities, electron temperature, etc.), and the evaluation of ion fluxes and velocities at the thruster exit allows estimates of thruster performance to be made. Ignoring the (negligible) contribution of neutrals, as well as the electron pressure and any ion beam divergence, the thrust and specific impulse are

$$T \;=\; M A_{\rm ch} \left[\Gamma_{\rm I^+} u_{\rm I^+} + 2\Gamma_{\rm I_2^+} u_{\rm I_2^+}\right]_{x=L_{\rm ch}}, \tag{31}$$

$$I_{\rm sp} \;=\; \frac{T}{Q_{\rm m} g_0}, \tag{32}$$

where $g_0$ is the gravitational acceleration at sea level. The propellant mass utilization efficiency is

$$\eta_{\rm m} \;=\; \frac{\left[\Gamma_{\rm I^+} + 2\Gamma_{\rm I_2^+}\right]_{x=L_{\rm ch}}}{2\Gamma_{\rm I_2,inj}}, \tag{33}$$

while the total anode thruster efficiency is defined as

$$\eta_{\rm T} \;=\; \frac{T^2}{2 Q_{\rm m} P_{\rm d}}, \tag{34}$$

where $P_{\rm d} = I_{\rm d} V_{\rm d}$ is the discharge power. Finally, the thrust-to-power ratio is simply $T/P_{\rm d}$.

## III. RESULTS

### A. SPT-100 reference case

To analyze the model solutions, we first run a reference case using typical parameters for the well-characterized SPT-100 thruster summarized in Table II, and which allows us to connect with previous works using noble gas propellants (see for example Refs. [31, 32]). In this first case, the iodine mass flow rate at the anode is entirely in the molecular state, which means that we do not account for any initial thermal dissociation within the gas injection system, although this could be important in some thrusters [59–61]. We will come back to this below.

TABLE III. Typical parameters used for the SPT-100 thruster.

| Parameter | Value |
|---|---|
| $R_{\text{out}}$ | 5 cm |
| $R_{\text{in}}$ | 3.5 cm |
| $L_{\text{ch}}$ | 2.5 cm |
| $B_{\text{max}}$ | 20 mT |
| $Q_{\text{m}}$ | 5 mg/s |
| $V_{\text{d}}$ | 250 V |

#### 1. *Performance comparison with xenon*

Table IV shows iodine thruster performance predictions from the model, as well as predictions for a xenon thruster previously calculated in Ref. [32]. Note that the present model, as with the model in Ref. [32], does not account for 2D effects and may therefore overestimate the performance because ion beam divergence is neglected. The typical beam divergence in a Hall thruster is of the order of 20-30 degrees [7], which would result in a divergence efficiency of 87-94%. For completeness, experimental measurements for the SPT-100 (operating with xenon) are also provided [62]. Overall, the performance with iodine and xenon propellants is comparable and consistent with the outcome of previous experimental testing [63]. This reference case however already highlights important results: (i) the thrust provided by

TABLE IV. Thruster performance obtained with iodine (this work) and xenon (see Ref. [32]) using the SPT-100 parameters in Table III. Experimental data for the SPT-100 operating with xenon at a discharge voltage of 250 V and a mass flow rate of 4.94 mg/s is also included for comparison [62]. For the iodine case, the thrust from $I_2^+$ is 21.9 mN while the thrust from $I^+$ is 48.7 mN.

| Parameter | Iodine | Xenon | Xenon (Exp.) |
|---|---|---|---|
| $I_\mathrm{d}$ (A) | 4.27 | 4.42 | 4.32 |
| Power (W) | 1063 | 1105 | 1080 |
| Total thrust (mN) | 70.6 | 70.7 | 68.1 |
| Specific impulse (s) | 1439 | 1441 | 1405 |
| Mass efficiency | 0.92 | 0.89 | - |
| Total efficiency | 0.47 | 0.45 | 0.43 |
| Thrust-to-power ratio (mN/kW) | 66.4 | 64 | 63.1 |

molecular ions can be significant and in the present case represents around 31% of the total thrust (the thrust from $I_2^+$ is 21.9 mN, while the thrust from $I^+$ is 48.7 mN), (ii) despite the significant amount of molecular ions, the specific impulse is comparable to xenon. To better understand these important results, we analyze the internal plasma discharge structure and composition in the next section.

### *2. Discharge structure and composition*

Figure 3 shows the axial profiles of all iodine species densities and fluxes, as well as the electron temperature, for the reference case in Table IV. The molecular neutral iodine flux rapidly decays along the thruster channel, reaching almost zero at the exit. Because of electron impact dissociation, the atomic iodine flux first increases from zero at the anode, reaches a maximum around $x = 0.012$ m, and then later decays due to ionization. We note that the atomic iodine flux is lower than the molecular iodine flux throughout a significant fraction of the discharge (up until about $x = 0.009$ m) and is not negligible at the exit.

Near the anode, the molecular iodine ion flux initially increases faster than the atomic iodine ion flux, and it remains higher until approximately the middle of the channel. The atomic iodine ion flux then subsequently becomes higher while the molecular iodine ion

flux saturates, and even begins to slightly decay because of electron impact dissociation. At the thruster exit, the molecular iodine ion flux represents about 22% of the total ion flux. This is consistent with recent global model results of an iodine Hall thruster [49]. Although experimental data for iodine Hall thrusters with an SPT-like design is sparse, on-axis measurements in the plume of a Busek BHT-200 Hall thruster suggest that the molecular iodine ion flux fraction is only a few percent, but may reach as high as 20% off-axis [64]. Because of ion-neutral charge-exchange and fragmentation reactions (such as $\mathrm{I}_2^+ + \mathrm{I} \longrightarrow \mathrm{I}_2 + \mathrm{I}^+$ and $\mathrm{I}_2^+ + \mathrm{I} \longrightarrow \mathrm{I}^+ + 2\mathrm{I}$) which are neglected in the model, and the distance between the thruster exit and probe measurement location in the experiments, a direct comparison is difficult. Nonetheless, these observations may indicate that beam divergence of molecular and atomic iodine ions is different.

The electron temperature profile is shown in the top-right subplot in Figure 3. The temperature is fairly low near the anode, which is most likely a consequence of the weak electric field in this location, the high molecular neutral density (see bottom-left subplot in Figure 3), and the reasonably low threshold energy for molecular ionization. Moving towards the thruster exit, the electron temperature increases monotonically before saturating at around 17 eV, largely because electron energy losses at the radial channel walls become extremely high due to intense SEE. Note that just before the thruster exit, the electron temperature starts to increase again because at this point the secondary electron emission yield has reached $\sigma = \sigma_{\mathrm{cr}}$. In the present case, this sudden increase in the electron temperature does not significantly affect the other profiles because it remains moderate and very near the exit, where almost complete molecular dissociation has occurred. At higher voltages, the region of high electron temperature moves further inward and the profiles are modified.

The neutral density profiles are essentially identical to the neutral flux profiles since the neutral species velocities are assumed constant in the model. By contrast, the charged-particle density profiles exhibit clear maxima as ions are accelerated downstream. The molecular ion density peaks around $x = 0.011$ m, while the atomic ion density peaks downstream at $x = 0.015$ m. The electron density, which is the sum of molecular and atomic ion densities, peaks in-between at $x = 0.013$ m and attains a maximum value just above $n_{\mathrm{e,\,max}} = 10^{18}$ m$^{-3}$.

Figure 4 shows the ion velocities as a function of position along the channel, as well as the electric field and ionization rate profiles. Although the molecular ion velocity is

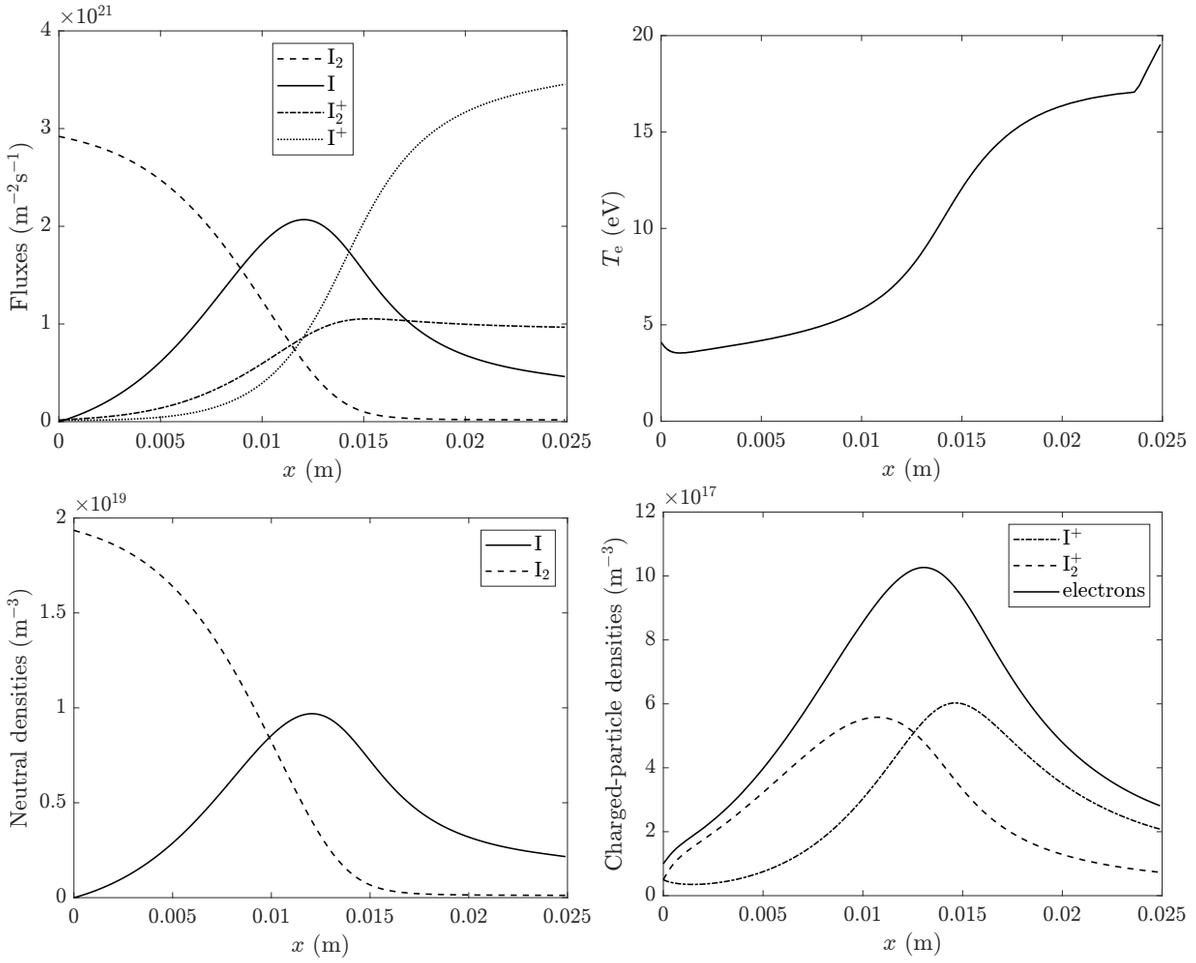


FIG. 3. Iodine species fluxes (top-left), electron temperature (top-right), neutral densities (bottom-left), and charged-particle densities (bottom-right) as a function of position along the thruster channel.

lower than the atomic ion velocity, we note somewhat surprisingly that the difference is not proportional to the square root of the mass ratio as might be expected. This can be understood by comparing the ionization and acceleration zones within the channel (right subplot in Figure 4). Here, we see a unique discharge structure with two distinct ionization zones (as also seen in [49]). Molecular ions are predominantly generated further upstream of the atomic ions and before the electric field magnitude increases significantly, while atomic ion generation overlaps more substantially with the acceleration zone. Consequently, the effective accelerating potential seen by molecular ions is higher than that for atomic ions, which partially compensates for the higher molecular mass and therefore gives more similar

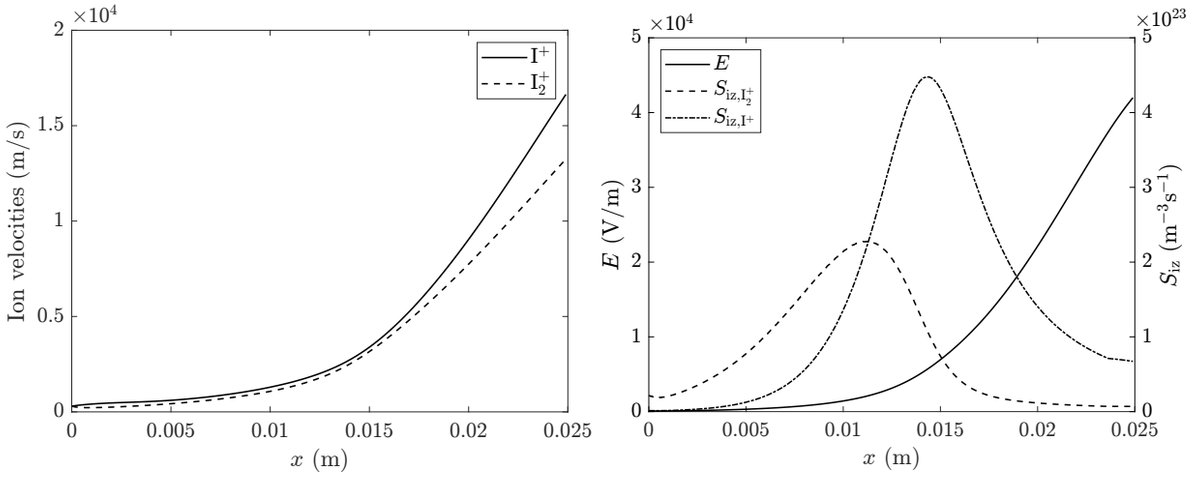


FIG. 4. Ion velocities (left), and electric field and ionization rate profiles (right) as a function of position along the thruster channel, with $S_{\mathrm{iz,I_2^+}} = n_\mathrm{e} n_{\mathrm{I}_2} K_{\mathrm{iz,I}_2}$ and $S_{\mathrm{iz,I^+}} = n_\mathrm{e} n_{\mathrm{I}_2} K_{\mathrm{diss.iz,I}_2} + n_\mathrm{e} n_\mathrm{I} K_{\mathrm{iz,I}}$

ion velocities. This important observation explains why the specific impulse is similar to xenon. The shift in ionization zones also suggests that the energy distribution of atomic ions in the plume will be broader than that of the molecular ions.

Figure 5 shows the spatial variation of the different terms contributing to the effective electron momentum transfer collision frequency in Eq. 18. As typically observed in Hall thrusters, anomalous transport dominates near the exit. However, we note that the terms due to elastic collisions are quite important and almost never negligible in the channel. This is particularly true for electron impact elastic collisions with molecular iodine, for which the reaction cross-section is larger than that of noble gases. This increases the electron mobility compared with xenon, and suggests that anomalous transport may be less important. We note though that no definitive conclusion can be drawn as anomalous transport has only been included with an empirical expression using a transport coefficient derived for xenon [32]. Previous PIC simulations have however indicated that anomalous transport is reasonably similar for different propellants [65].

As briefly highlighted above, iodine may be significantly dissociated in the gas injection system and it is useful to analyze this effect with the present model. If one considers static thermodynamic equilibrium (i.e. without significant gas flow), the dissociation degree, defined as $\alpha = n_\mathrm{I}/(n_\mathrm{I} + 2n_{\mathrm{I}_2})$, is 0.35 at $T_\mathrm{g} = 700$ K and drops to 0.136 at $T_\mathrm{g} = 650$ K in our conditions. In a real system, even if some parts of the anode are at 700 K, other parts may be

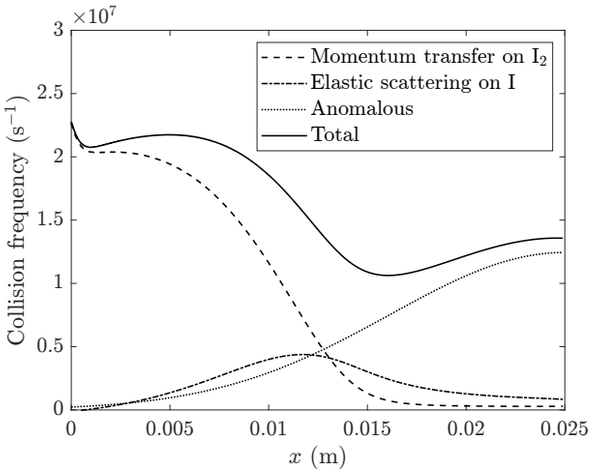


FIG. 5. Spatial variation of the different terms in the electron effective momentum transfer collision frequency used in Eq. 18.

at a lower temperature. Furthermore, depending on the injector design, the gas temperature may anyway not necessarily be equal to the anode temperature (such as if the gas flow speed is high). Nonetheless, to evaluate the thermal dissociation effect, we have run a case with a significant dissociation degree at the anode ($\alpha = 0.13$), and generated in figure 6 the same profiles as those in figure 3. As can be seen, the flux profiles are affected, but the overall discharge structure remains fairly similar. Even more importantly, the performance metrics are almost unaffected compared to the results shown in table IV, with a total thrust of 71.9 mN (instead of 70.6), a specific impulse of 1446 s (instead of 1441 s) and a similar total efficiency at 0.47. The molecular iodine ion flux fraction at the thruster exit is somewhat smaller at 17.5% (compared to 22% in the reference case). In the following, all calculations will therefore be performed without thermal dissociation at the anode.

### B. Effect of mass flow rate at constant voltage

We now use the model to explore the effect of the main operating parameters on thruster performance. Figure 7 shows the discharge current, thrust, anode specific impulse, and anode thruster efficiency as a function of mass flow rate for a discharge voltage of 250 V. The results for xenon obtained with the model in Ref. [32] are also shown for comparison. Since the discharge voltage is fixed, the discharge power increases with mass flow rate. In the case of iodine, the discharge power varies from less than 100 W to just under 2000 W as

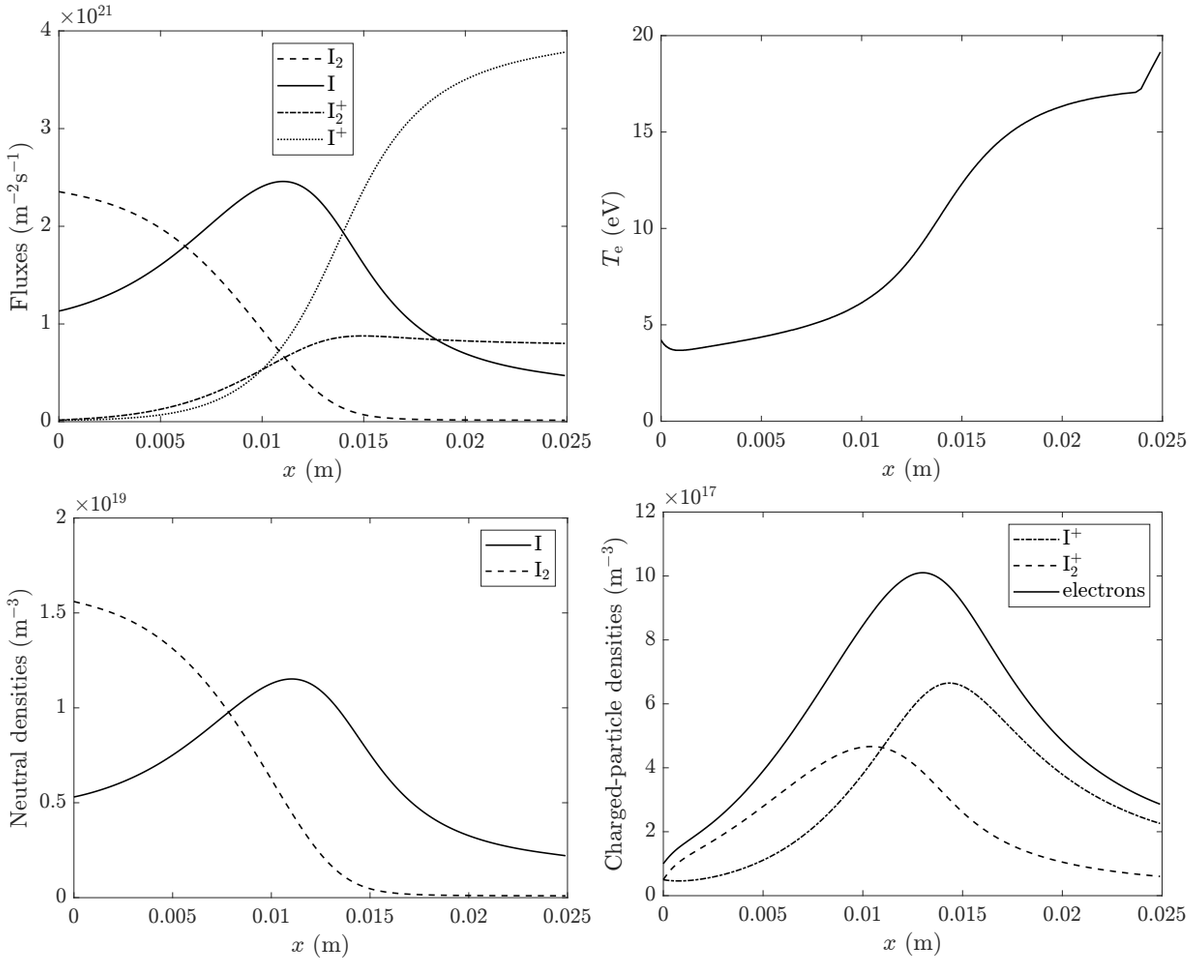


FIG. 6. Iodine species fluxes (top-left), electron temperature (top-right), neutral densities (bottom-left), and charged-particle densities (bottom-right) as a function of position along the thruster channel. The conditions are identical to those in figure 3, except that in the present case, iodine is injected with a significant fraction of atoms, to account for possible thermal dissociation in the gas inlet anodic region.

the mass flow rate varies from 1 mg/s to 8 mg/s. For both iodine and xenon, the discharge current and thrust increase almost linearly with mass flow rate (consistent with experimental measurements; see for example Ref. [11]), while the specific impulse and thruster efficiency initially increase sharply at low mass flow rates before leveling off at higher flow rates. As seen, the performance of iodine and xenon are comparable at moderate-to-high mass flow rates. However, there are strong differences at low mass flow rates with iodine exhibiting significantly better performance. These results are again consistent with several experiments

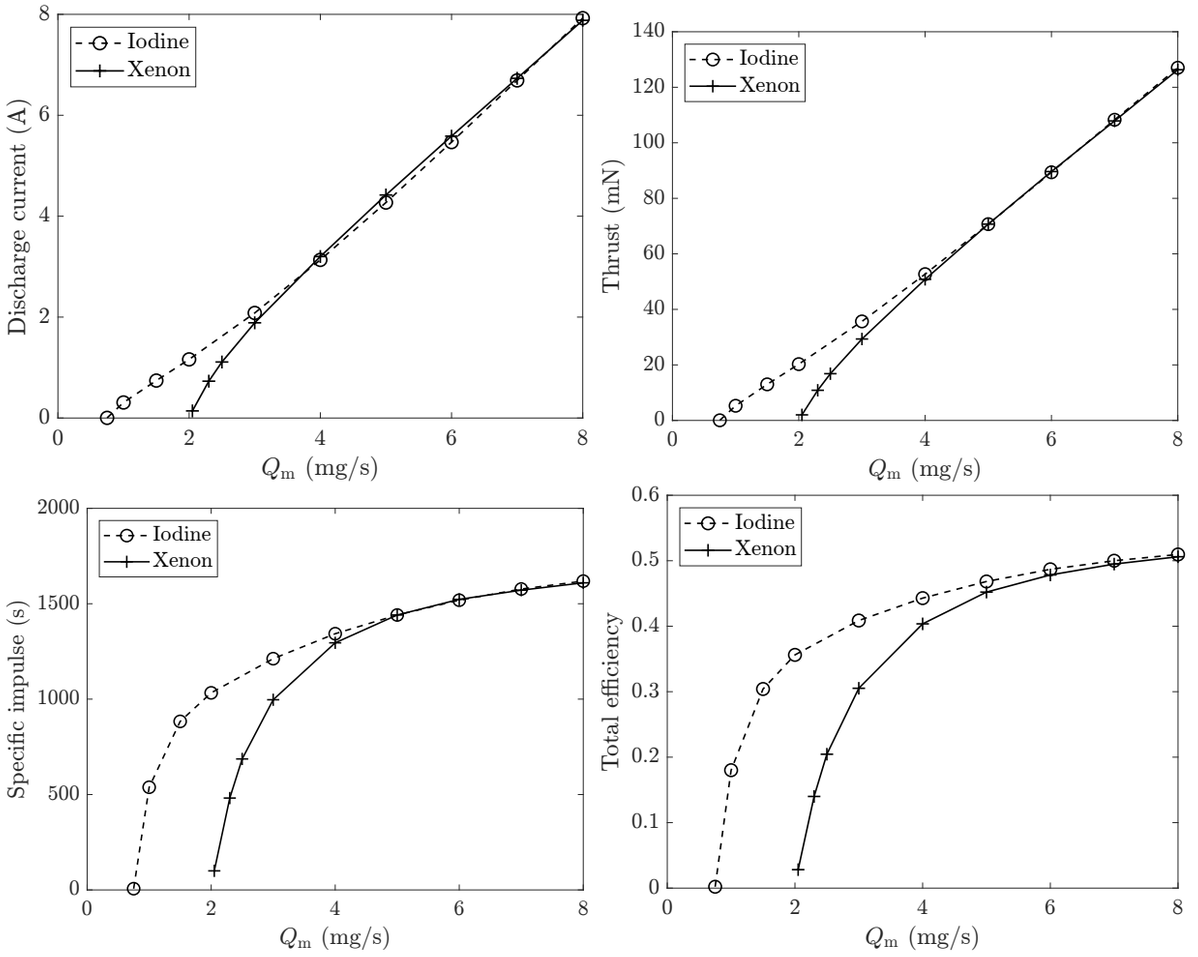


FIG. 7. Discharge current (top-left), thrust (top-right), anode specific impulse (bottom-left) and anode thruster efficiency (bottom-right) as a function of propellant mass flow rate. The discharge voltage is 250 V.

[11]. From an operational perspective, an iodine Hall thruster can therefore function over a broader mass flow rate and discharge power range.

The molecular iodine ion flux fraction at the thruster exit, $\Gamma_{I_2^+}/(\Gamma_{I^+} + \Gamma_{I_2^+})$, is shown in Figure 8 as a function of mass flow rate. The flux fraction is just above 90% at the lowest mass flow rate of 0.75 mg/s and decays to about 10% at 8 mg/s, which is correlated with the increase in discharge current, discharge power, and thruster efficiency (see Figure 7). Indeed, the discharge current increases from less than 1 A at 1 mg/s to almost 8 A at 8 mg/s. Similarly, the maximum electron density in the channel increases from around $2.7 \times 10^{17}$ m$^{-3}$ at 1 mg/s to about $1.9 \times 10^{18}$ m$^{-3}$ at 8 mg/s. This is roughly consistent

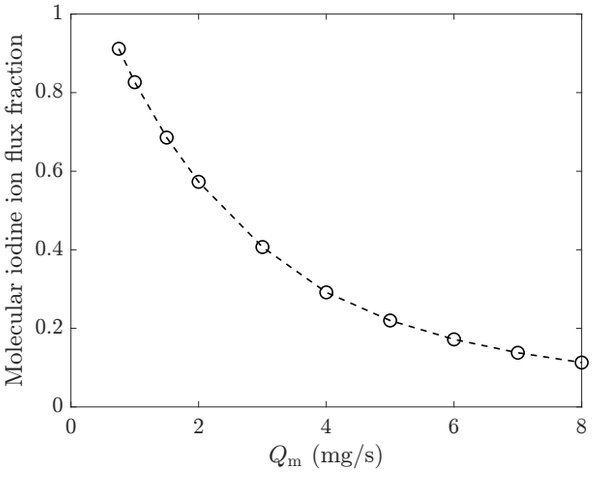


FIG. 8. Molecular iodine ion flux fraction, $\Gamma_{I_2^+}/(\Gamma_{I^+}+\Gamma_{I_2^+})$, as a function of iodine propellant mass flow rate. The discharge voltage is 250 V.

with the analytical result in Ref. [31] where the maximum density was shown to scale almost linearly with discharge current. This point will be discussed further below. A higher electron density then leads to a higher dissociation rate of molecular iodine that in turn favors a higher production rate of atomic ions by direct ionization (due to an increased atomic iodine density). Consequently, when operated at high efficiency conditions, the fraction of molecular ions is much reduced (qualitatively inline with the experiments in Ref. [63]).

### C. Effect of discharge voltage at constant mass flow rate

Figure 9 shows the discharge current, thrust, anode specific impulse, and anode thruster efficiency as a function of discharge voltage for a fixed mass flow rate of 5 mg/s. The results for xenon from the model in Ref. [32] are again shown for comparison. The discharge current-voltage characteristic exhibits the usual behavior with a minimum required voltage needed to initiate and sustain the discharge [66], followed by a sharp increase in current as the voltage is increased, and then a saturation at higher voltages. We note however that the model current does not fully saturate at high voltages, nor is there a local maximum observed at intermediate voltages (as is often found experimentally [66]). This is a consequence of the simplified phenomenological anomalous electron transport model (see [31] and [32]) . The dashed and solid horizontal lines in the top-left subplot of Figure 9 shows the maximum ion

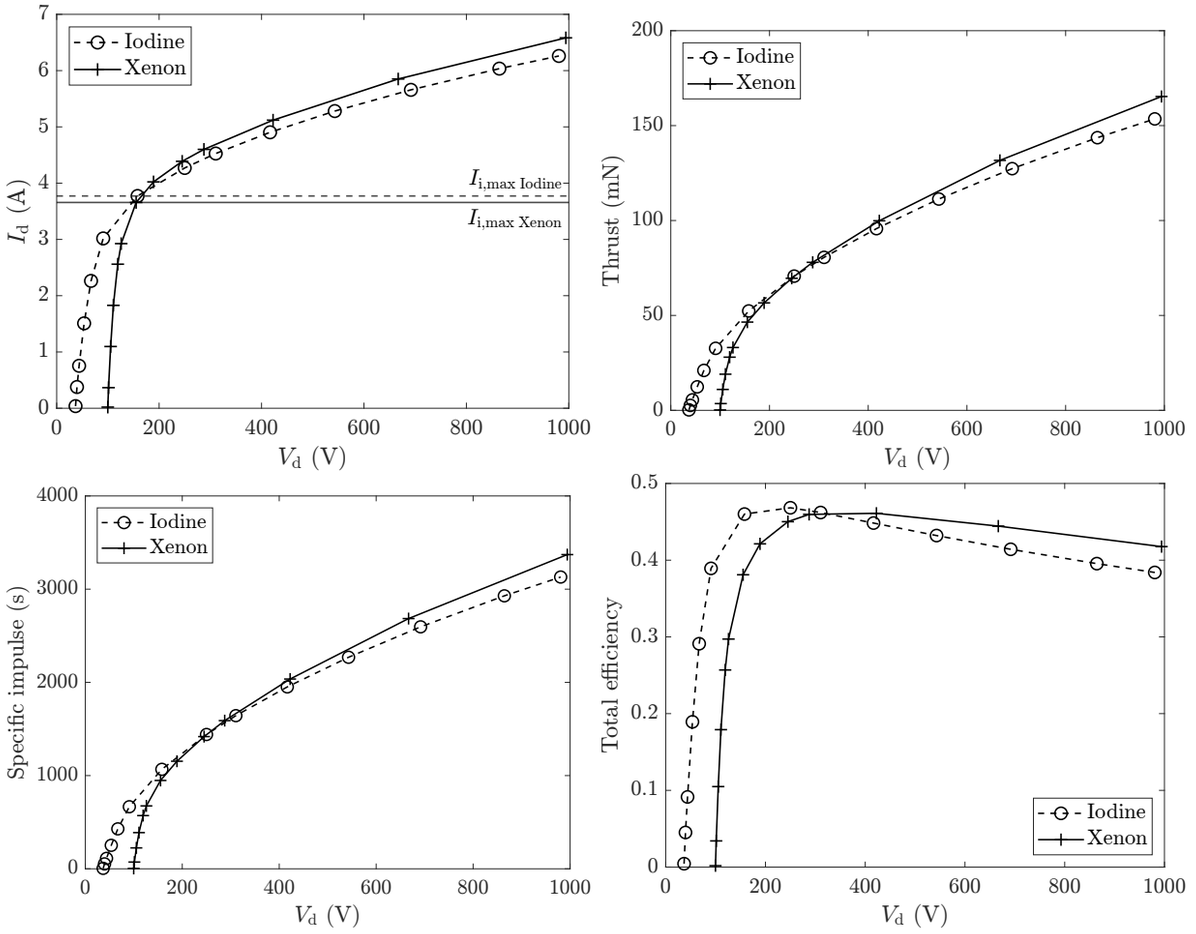


FIG. 9. Discharge current (top-left), thrust (top-right), anode specific impulse (bottom-left), and anode thruster efficiency (bottom-right) as a function of discharge voltage. The mass flow rate is 5 mg/s and the maximum ion current for both propellant is defined as $I_{\mathrm{i,max}} \equiv eQ_{\mathrm{m}}/M$.

current, $I_{\mathrm{i,max}}$, for both iodine and xenon: i.e. the ion current that would be obtained if all input propellant was fully ionized into singly-charged atomic ions. The slight difference in maximum currents is because of the small mass difference between atomic iodine and xenon. Both the thrust and specific impulse increase monotonically with discharge voltage as expected, while the thruster efficiency displays a local maximum between 200-250 V for iodine, and 300-350 V for xenon. Although the performance with iodine and xenon is comparable, we again observe that iodine is better at low voltages, and has a lower sustainment voltage. This suggests that thruster ignition may be easier with iodine.

Figure 10 shows the molecular iodine ion flux fraction at the thruster exit as a function of discharge voltage. A sharp decay in molecular ion fraction is initially observed as the

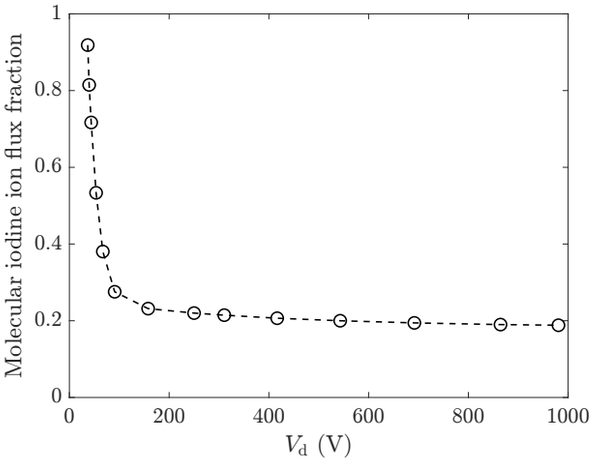


FIG. 10. Molecular iodine ion flux fraction, $\Gamma_{I_2^+}/(\Gamma_{I^+} + \Gamma_{I_2^+})$, as a function of discharge voltage. The iodine mass flow rate is 5 mg/s.

voltage is increased, but at higher voltages the ion fraction again plateaus and reaches a value just below 20%. As seen in the top-left subplot in Figure 9, the discharge current does not increase linearly with voltage, and the maximum electron density at around 6 A (corresponding to a voltage of 900 V) is only about $1.2 \times 10^{18}$ m$^{-3}$: i.e. smaller than that obtained previously for 8 mg/s at 250 V. This explains why saturation of the ion flux fraction is around 20% instead of 10% (see Figure 8) despite a power consumption of about 5400 W compared with 2000 W. Importantly therefore, the molecular ion fraction is connected with the discharge current and not the discharge power. As discussed in Sec. III B, this is because the maximum electron density scales almost linearly with discharge current [31], and if the electron density increases, so too does the dissociation rate. To better illustrate this, figure 11 shows the maximum electron density (left) and the molecular iodine ion flux fraction, $\Gamma_{I_2^+}/(\Gamma_{I^+} + \Gamma_{I_2^+})$, (right), as a function of discharge current. The two curves are obtained from the datasets presented above at constant voltage (250 V) and at constant mass flow rate (5 mg/s). Despite the discharge power being different in these two dataset, both the maximum electron density and the molecular iodine ion flux fraction are almost identical, demonstrating that they depend almost uniquely on the discharge current.

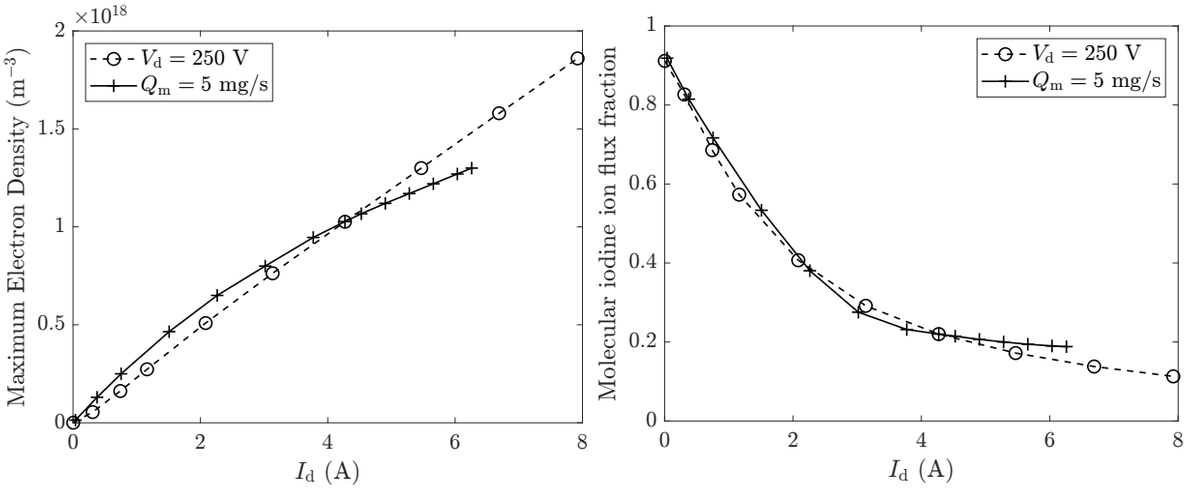


FIG. 11. Maximum electron density (left) and molecular iodine ion flux fraction, $\Gamma_{I_2^+}/(\Gamma_{I^+} + \Gamma_{I_2^+})$, (right), as a function of discharge current.

## IV. CONCLUSIONS

In summary, a time-independent, one-dimensional, fluid model previously developed for noble gas propellants has been extended to iodine. The model accounts for radial plasma-wall losses, wall recombination, SEE, and anomalous electron transport using a simplified empirical expression. The iodine plasma chemistry set includes several important reactions and the model explicitly considers molecular and atomic iodine, as well as molecular and atomic iodine ions. Negative ions, which may play a role in the near-anode region, were not considered, nor doubly-charged atomic ions. The model was applied to a representative SPT-100 Hall thruster geometry (optimized for xenon), and comparable performance was found for iodine and xenon as the discharge voltage and propellant mass flow rate were varied. However, it is found that performance is better with iodine at both lower mass flow rates and lower voltages than xenon, and that the discharge can operate over a much wider range. When operated at low power, the fraction of molecular ions in the beam is significant and they contribute substantially to the thrust. It has been shown that the ion fraction is directly linked to the maximum electron density in the channel, which is almost proportional to the discharge current. Consequently, at high discharge currents (and therefore high electron densities), the fraction of molecular ions is much smaller, although never negligible for the cases studied here. Finally, we note that because significant fractions

of both molecular and atomic ions are expected to be present in iodine-fueled Hall thrusters, axial ion streaming instabilities may be excited and affect discharge operation [67].

In future work, this model could be extended to include doubly-charged ions that may be present in significant quantities for some conditions, such as for high voltage operation. The breathing mode dynamics, known as an important aspect of Hall thrusters, could be implemented in a time-varying one-dimensional fluid model using the same chemistry set. However, the equations will have to be solved as a boundary value problem with different numerical algorithms. This would allow the electron-pressure and the negative ion terms to be included, leading to a better description of the anodic region. Eventually, PIC simulations in iodine will have to be developed for higher fidelity calculations, in particular to investigate anomalous transport.

## ACKNOWLEDGMENTS

The author would like to thank Dr Cyril Drag for very useful discussions on thermal iodine dissociation. The work was partially supported by Agence de l'Innovation de Défense – AID - via Centre Interdisciplinaire d'Etudes pour la Défense et la Sécurité – CIEDS - (project 2023 – VALIDHETION).

## APPENDIX

As indicated in the body of the paper, the model reduces to five differential equations and three algebraic equation, two of which are conservation laws, to be solved for six variables. Among several possible choices, we have used the six following variables,

$$\Gamma_{\rm g} = \Gamma_{\rm I_2} \tag{35}$$

$$\Gamma_1 = \Gamma_{\rm I^+} \tag{36}$$

$$\Gamma_2 = \Gamma_{\rm I_2^+} \tag{37}$$

$$\mathrm{G}_1 = \Gamma_{\rm I^+} v_{\rm I^+} \tag{38}$$

$$\mathrm{G}_2 = \Gamma_{\rm I_2^+} v_{\rm I_2^+} \tag{39}$$

$$E = \frac{\Gamma_{\rm d} - \Gamma_2 - \Gamma_1}{n_{\rm e}\mu} \tag{40}$$

from which the densities are easily expressed, as follows:

$$n_{\mathrm{I}_2} = \frac{\Gamma_{\mathrm{g}}}{v_{\mathrm{I}_2}} \tag{41}$$

$$n_{\mathrm{I}} = \frac{2\Gamma_{\mathrm{m}} - 2\Gamma_{\mathrm{g}} - 2\Gamma_2 - \Gamma_1}{v_{\mathrm{I}}} \tag{42}$$

$$n_{\mathrm{I}^+} = \frac{\Gamma_1^2}{\mathrm{G}_1} = n_1 \tag{43}$$

$$n_{\mathrm{I}_2^+} = \frac{\Gamma_2^2}{\mathrm{G}_2} = n_2 \tag{44}$$

$$n_{\mathrm{e}} = \frac{\Gamma_1^2}{\mathrm{G}_1} + \frac{\Gamma_2^2}{\mathrm{G}_2} \tag{45}$$

With these new variables, the five ordinary differential equations (ode's) to be integrated numerically become

$$\begin{aligned}\frac{\mathrm{d}\Gamma_{\mathrm{g}}}{\mathrm{d}x} &= -n_{\mathrm{e}} n_{\mathrm{I}_2} \left(K_{\mathrm{iz,I}_2} + K_{\mathrm{diss.iz,I}_2} + K_{\mathrm{diss,I}_2}\right) \\ &+ \frac{1}{4} n_{\mathrm{I}} \sqrt{\frac{8}{\pi}} v_{\mathrm{I}} \left(\frac{2\gamma}{2-\gamma}\right)\left(\frac{1}{\Delta R}\right) + \frac{2h_R n_2 u_{\mathrm{B,I}_2^+}}{\Delta R}, \end{aligned} \tag{46}$$

$$\frac{\mathrm{d}\Gamma_2}{\mathrm{d}x} = n_{\mathrm{e}} n_{\mathrm{I}_2} K_{\mathrm{iz,I}_2} - n_{\mathrm{e}} n_2 K_{\mathrm{diss,I}_2^+} - \frac{2h_R n_2 u_{\mathrm{B,I}_2^+}}{\Delta R}, \tag{47}$$

$$\frac{\mathrm{d}\Gamma_1}{\mathrm{d}x} = n_{\mathrm{e}} n_{\mathrm{I}} K_{\mathrm{iz,I}} + n_{\mathrm{e}} n_{\mathrm{I}_2} K_{\mathrm{diss.iz,I}_2} + n_{\mathrm{e}} n_2 K_{\mathrm{diss,I}_2^+} - \frac{2h_R n_1 u_{\mathrm{B,I}^+}}{\Delta R}, \tag{48}$$

$$\frac{\mathrm{dG}_2}{\mathrm{d}x} = \frac{e n_2 E}{2M} - \frac{2h_R n_2 u_{\mathrm{B,I}_2^+}}{\Delta R} \frac{\mathrm{G}_2}{\Gamma_2}, \tag{49}$$

$$\frac{\mathrm{dG}_1}{\mathrm{d}x} = \frac{e n_1 E}{M} - \frac{2h_R n_1 u_{\mathrm{B,I}^+}}{\Delta R} \frac{\mathrm{G}_1}{\Gamma_1}, \tag{50}$$

where we have not substituted the densities, defined by Eqs. (41-45), for readability. The (algebraic) electron power balance remains unchanged,

$$\mu E^2 = \nu_{\mathrm{wall}} \varepsilon_{\mathrm{wall}} + n_{\mathrm{I}} K_{\mathrm{iz,I}} \varepsilon_{\mathrm{c,I}} + n_{\mathrm{I}_2} \left(K_{\mathrm{iz,I}_2} + K_{\mathrm{diss.iz,I}_2}\right) \varepsilon_{\mathrm{c,I}_2}, \tag{51}$$

and must be solved at each integration step to obtain the electron temperature, and in turns the wall energy loss, the collisional energy loss terms, and the various reaction rates.

The model is solved as an initial value problem, using a commercial ordinary differential equation (ode) integrator; we routinely used the ode23s Matlab integrator but other solvers, such as the Matlab ode45 and the Python SciPy Library odeint, gave the same answer within less than 1%.

The integration requires initial values (at the anode) for the five variables appearing in the ode's: $\Gamma_{\mathrm{g}}$, $\Gamma_1$, $\Gamma_2$, $\mathrm{G}_1$ and $\mathrm{G}_2$. For the reference case in section III.A, we use the following

initial values

$$\Gamma_{\mathrm{m}} = 2.9428 \times 10^{21}\,\mathrm{m^{-2}s} \tag{52}$$

$$\Gamma_{10} = 1.5 \times 10^{19}\,\mathrm{m^{-2}s^{-1}} \tag{53}$$

$$\Gamma_{20} = 1.5 \times 10^{19}\,\mathrm{m^{-2}s^{-1}} \tag{54}$$

$$\Gamma_{\mathrm{g0}} = (2\Gamma_{\mathrm{m}} - 2\Gamma_{20} - \Gamma_{10})/2 \tag{55}$$

$$\mathrm{G}_{10} = 4.5 \times 10^{21}\,\mathrm{m^{-1}s^{-2}} \tag{56}$$

$$\mathrm{G}_{20} = 4.5 \times 10^{21}\,\mathrm{m^{-1}s^{-2}} \tag{57}$$

Note that we used $\Gamma_{\mathrm{g0}} = 0.8 \times (2\Gamma_{\mathrm{m}} - 2\Gamma_{20} - \Gamma_{10})/2)$ for the case in figure 6 with thermal dissociation.

Different initial values could be used without varying significantly the quantities at the channel exit but leading to different initial $T_{\mathrm{e}}$ and electric field profiles near $x = 0$. In particular, when varying considerably the operating regimes in sections III. B and III. C it was necessary to adjust the initial conditions to make sure that the initial $T_e$ and electric field were reasonable.

## REFERENCES

[1] Satellites to be built and launched by 2029, market research report, Euroconsult, 2021.

[2] T. J. Logue and J. Pelton, Overview of Commercial Small Satellite S ystems in the "New Space" Age, in *Handbook of Small Satellites: Technology, Design, Manufacture, Applications, Economics and Regulation*, edited by J. Pelton (Springer International Publishing, Cham, 2019) pp. 1–18.

[3] R. Sandau, Status and trends of small satellite missions for Earth observation, acta astronautica **66**, 1 (2010).

[4] J. C. McDowell, The low earth orbit satellite population and impacts of the SpaceX Starlink constellation, The Astrophysical Journal Letters **892**, L36 (2020).

[5] E. Lagunas, S. Chatzinotas, and B. Ottersten, Low-Earth orbit satellite constellations for global communication network connectivity, Nature Reviews Electrical Engineering **1**, 656 (2024).

[6] D. Lev, R. M. Myers, K. M. Lemmer, J. Kolbeck, H. Koizumi, and K. Polzin, The technological and commercial expansion of electric propulsion, Acta Astronautica **159**, 213 (2019).

[7] D. M. Goebel, I. Katz, and I. G. Mikellides, *Fundamentals of electric propulsion* (John Wiley & Sons, 2023).

[8] V. V. Zhurin, H. R. Kaufman, and R. S. Robinson, Physics of closed drift thrusters, Plasma Sources Science and Technology **8**, R1 (1999).

[9] J. Szabo, M. Robin, S. Paintal, B. Pote, and V. Hruby, High density Hall thruster propellant investigations, in *48th AIAA/ASME/SAE/ASEE Joint Propulsion Conference & Exhibit* (2012) p. 3853.

[10] B. Jorns and T. Lafleur, Foundations of plasmas as ion sources, Plasma Sources Science and Technology **32**, 014001 (2023).

[11] V.-G. Tirila, A. Demairé, and C. N. Ryan, Review of alternative propellants in Hall thrusters, Acta Astronautica **212**, 284 (2023).

[12] K. Dannenmayer and S. Mazouffre, Elementary scaling relations for Hall effect thrusters, Journal of Propulsion and Power **27**, 236 (2011).

[13] A. A. Shagayda, On scaling of Hall effect thrusters, IEEE Transactions on Plasma Science **43**, 12 (2014).

[14] I. D. Kaganovich, A. Smolyakov, Y. Raitses, E. Ahedo, I. G. Mikellides, B. Jorns, F. Taccogna, R. Gueroult, S. Tsikata, A. Bourdon, J.-P. Boeuf, M. Keidar, A. T. Powis, M. Merino, M. Cappelli, K. Hara, J. A. Carlsson, N. J. Fisch, P. Chabert, I. Schweigert, T. Lafleur, K. Matyash, A. V. Khrabrov, R. W. Boswell, and A. Fruchtman, Physics of E×B discharges relevant to plasma propulsion and similar technologies, Physics of Plasmas **27**, 120601 (2020).

[15] D. Sydorenko, A. Smolyakov, I. Kaganovich, and Y. Raitses, Kinetic simulation of secondary electron emission effects in Hall thrusters, Physics of Plasmas **13**, 014501 (2006).

[16] J. Adam, A. Héron, and G. Laval, Study of stationary plasma thrusters using two-dimensional fully kinetic simulations, Physics of Plasmas **11**, 295 (2004).

[17] T. Lafleur, S. D. Baalrud, and P. Chabert, Theory for the anomalous electron transport in Hall effect thrusters. I. Insights from particle-in-cell simulations, Physics of Plasmas **23**, 053502 (2016).

[18] T. Lafleur and P. Chabert, The role of instability-enhanced friction on 'anomalous' electron and ion transport in Hall-effect thrusters, Plasma Sources Science and Technology **27**, 015003 (2017).

[19] I. G. Mikellides, A. Lopez Ortega, and V. H. Chaplin, Theory of the anomalous momentum exchange from wave–particle interactions in Hall-effect ion accelerators and comparisons with measurements, Physics of Fluids **36**, 074121 (2024).

[20] J. Boeuf and L. Garrigues, Low frequency oscillations in a stationary plasma thruster, Journal of applied physics **84**, 3541 (1998).

[21] J. W. Koo and I. D. Boyd, Modeling of anomalous electron mobility in Hall thrusters, Physics of Plasmas **13**, 033501 (2006).

[22] S. Barral and E. Ahedo, Low-frequency model of breathing oscillations in Hall discharges, Physical Review E—Statistical, Nonlinear, and Soft Matter Physics **79**, 046401 (2009).

[23] G. Hagelaar, J. Bareilles, L. Garrigues, and J.-P. Boeuf, Role of anomalous electron transport in a stationary plasma thruster simulation, Journal of Applied Physics **93**, 67 (2003).

[24] I. G. Mikellides and I. Katz, Numerical simulations of Hall-effect plasma accelerators on a magnetic-field-aligned mesh, Physical Review E **86**, 046703 (2012).

[25] T. Lafleur, S. D. Baalrud, and P. Chabert, Theory for the anomalous electron transport in

Hall effect thrusters. II. Kinetic model, Physics of Plasmas **23**, 053503 (2016).

[26] T. Lafleur, P. Chabert, and A. Bourdon, The origin of the breathing mode in Hall thrusters and its stabilization, Journal of Applied Physics **130**, 053305 (2021).

[27] E. Ahedo, P. Martınez-Cerezo, and M. Martınez-Sánchez, One-dimensional model of the plasma flow in a Hall thruster, Physics of plasmas **8**, 3058 (2001).

[28] A. Cohen-Zur, A. Fruchtman, J. Ashkenazy, and A. Gany, Analysis of the steady-state axial flow in the Hall thruster, Physics of Plasmas **9**, 4363 (2002).

[29] E. Bello-Benítez and E. Ahedo, Stationary axial model of the Hall thruster plasma discharge: electron azimuthal inertia and far plume effects, Plasma Sources Science and Technology **32**, 115011 (2023).

[30] A. A. Shagayda and O. A. Gorshkov, Hall-thruster scaling laws, Journal of Propulsion and Power **29**, 466 (2013).

[31] T. Lafleur and P. Chabert, Analytical model of a Hall thruster, Physics of Plasmas **31**, 093507 (2024).

[32] T. Lafleur and P. Chabert, Similarity parameters and scaling laws for hall thrusters, Plasma Sources Science and Technology **34**, 055005 (2025).

[33] D. A. Herman and K. G. Unfried, Xenon acquisition strategies for high-power electric propulsion nasa missions, in *JANNAF SPS Subcommittee Meeting*, GRC-E-DAA-TN23198 (2015).

[34] "Russia's invasion of ukraine impacts gas markets critical to chip production", https://www.csis.org/blogs/perspectives-innovation/russias-invasion-ukraine-impacts-gas-markets-critical-chip-production, retrieved on may 7, 2024.

[35] D. Rafalskyi, J. M. Martínez, L. Habl, E. Zorzoli Rossi, P. Proynov, A. Boré, T. Baret, A. Poyet, T. Lafleur, S. Dudin, *et al.*, In-orbit demonstration of an iodine electric propulsion system, Nature **599**, 411 (2021).

[36] T. F. Munro-O'Brien and C. N. Ryan, Performance of a low power Hall effect thruster with several gaseous propellants, Acta Astronautica **206**, 257 (2023).

[37] R. Dressler, Y.-H. Chiu, and D. Levandier, Propellant alternatives for ion and Hall effect thrusters, in *38th Aerospace sciences meeting and exhibit* (2000) p. 602.

[38] O. Tverdokhlebov and A. Semenkin, Iodine propellant for electric propulsion-to be or not to be, in *37th Joint propulsion conference and exhibit* (2001) p. 3350.

[39] B. Esteves, R. Vicol, B. Laurent, O. Duchemin, T. V. Tsankov, F. Petronio, A. Alvarez La-

guna, A. Bourdon, C. Drag, and P. Chabert, Iodine ($I_2$) and noble gases (Xe, Kr, Ar) plasma physics for HETs with preliminary characterisation of the PPS®X00 running on these alternative propellants, in *38th International Electric Propulsion Conference, Toulouse, France* (2024) p. 559.

[40] J. Szabo, M. Robin, J. Duggan, and R. R. Hofer, Light metal propellant Hall thrusters, in *31st International Electric Propulsion Conference* (2009) pp. 2009–138.

[41] "Iodine", mineral commodity summaries, U.S. Geological Survey, january 2024.

[42] J. Szabo, B. Pote, S. Paintal, M. Robin, G. Kolencik, A. Hillier, R. Branam, and R. Huffman, Performance Evaluation of an Iodine Vapor Hall thruster, in *47th AIAA/ASME/SAE/ASEE Joint Propulsion Conference & Exhibit* (2011) p. 5891.

[43] J. Dankanich, H. Kamhawi, M. W. Selby, and L. Byrne, The iodine satellite (iSat) project development through critical design review (cdr), in *52nd AIAA/SAE/ASEE Joint Propulsion Conference* (2016) p. 4540.

[44] G. F. Benavides, H. Kamhawi, J. Mackey, T. Haag, and G. Costa, Iodine Hall-effect electric propulsion system research, development, and system durability demonstration, in *2018 Joint Propulsion Conference* (2018) p. 4422.

[45] O. Jia-Richards and T. Lafleur, Iodine Electric Propulsion System Thrust Validation: From Numerical Modeling to In-Space Testing, Journal of Propulsion and Power **39**, 896 (2023).

[46] H. B. Ambalampitiya, K. R. Hamilton, O. Zatsarinny, K. Bartschat, M. A. Turner, A. Dzarasova, and J. Tennyson, Electron scattering cross-section calculations for atomic and molecular iodine, Atoms **9**, 103 (2021).

[47] B. Esteves, *Investigation of iodine plasmas for space propulsion applications*, Ph.D. thesis, Institut polytechnique de Paris (2022).

[48] J.-P. Boeuf, Tutorial: Physics and modeling of Hall thrusters, Journal of Applied Physics **121**, 011101 (2017).

[49] F. M. Bianchi, A. E. Vinci, and L. Garrigues, Global modeling of iodine Hall thruster performance and discharge properties, Journal of Applied Physics **137**, 043301 (2025).

[50] P. Grondein, T. Lafleur, P. Chabert, and A. Aanesland, Global model of an iodine gridded plasma thruster, Physics of Plasmas **23**, 033514 (2016).

[51] F. Marmuse, *Iodine plasmas: experimental and numerical studies. Application to electric propulsion*, Ph.D. thesis, Sorbonne Université (2020).

[52] B. Esteves, C. Drag, A. Bourdon, and A. Alvarez-Laguna, Experimental and numerical investigation of a gridded ion thruster running with different propellants ($I_2$, Xe, Kr, Ar), in *International Electric Propulsion Conference, Massachusetts Institute of Technology, Cambridge, MA, USA* (2022) p. 416.

[53] T. Lafleur, L. Habl, E. Z. Rossi, and D. Rafalskyi, Development and validation of an iodine plasma model for gridded ion thrusters, Plasma Sources Science and Technology **31**, 114001 (2022).

[54] K. Dannenmayer and S. Mazouffre, Sizing of Hall effect thrusters with input power and thrust level: an empirical approach, Journal of Technical Physics **49**, 231 (2008).

[55] P. Chabert and N. Braithwaite, *Physics of radio-frequency plasmas* (Cambridge University Press, 2011).

[56] S. Baalrud, C. Hegna, and J. Callen, Instability-Enhanced Collisional Friction Can Determine the Bohm Criterion in Multiple-Ion-Species Plasmas, Physical review letters **103**, 205002 (2009).

[57] S. D. Baalrud, T. Lafleur, W. Fox, and K. Germaschewski, Instability-enhanced friction in the presheath of two-ion-species plasmas, Plasma Sources Science and Technology **24**, 015034 (2015).

[58] G. Hobbs and J. Wesson, Heat flow through a Langmuir sheath in the presence of electron emission, Plasma Physics **9**, 85 (1967).

[59] M. M. Saravia, L. Bernazzani, A. Ceccarini, A. E. Vinci, and F. Paganucci, Modeling and characterization of a thermally controlled iodine feeding system for electric propulsion applications, Aerospace **7**, 10.3390/aerospace7020010 (2020).

[60] F. M. B. Alfio E. Vinci and D. Rafalskyi, Modeling and experimental results of low-power iodine-fed hall thruster propulsion system, in *IEPC Conference*, IEPC-2024-121 (2024).

[61] A. E. Vinci, Injection temperature and scheme effects on neutral flow dynamics in hall thrusters, Journal of Propulsion and Power **0**, 1 (2025), https://doi.org/10.2514/1.B39487.

[62] J. M. Sankovic, J. A. Hamley, and T. W. Haag, Performance evaluation of the Russian SPT-100 thruster at NASA LeRC, in *IEPC Conference*, IEPC-93-094 (1994).

[63] J. Szabo, B. Pote, S. Paintal, M. Robin, A. Hillier, R. D. Branam, and R. E. Huffmann, Performance evaluation of an iodine-vapor Hall thruster, Journal of Propulsion and Power **28**, 848 (2012).

[64] J. Szabo, M. Robin, S. Paintal, B. Pote, V. Hruby, and C. Freeman, Iodine propellant space propulsion, in *The 33rd International Electric Propulsion Conference (The George Washington University, USA, 6-10 October 2013). IEPC Paper*, Vol. 311 (2013).

[65] V. Croes, A. Tavant, R. Lucken, R. Martorelli, T. Lafleur, A. Bourdon, and P. Chabert, The effect of alternative propellants on the electron drift instability in Hall-effect thrusters: Insight from 2D particle-in-cell simulations, Physics of Plasmas **25**, 063522 (2018).

[66] V. Kim, Main physical features and processes determining the performance of stationary plasma thrusters, Journal of propulsion and power **14**, 736 (1998).

[67] S. Tsikata, J. Cavalier, A. Héron, C. Honoré, N. Lemoine, D. Grésillon, and D. Coulette, An axially propagating two-stream instability in the Hall thruster plasma, Physics of Plasmas **21**, 072116 (2014).